Gains Maximization via Impedance Matching Networks for Wireless Power Transfer

Qinghua Wang[1], Wenquan Che[1, *], Marco Dionigi[2],
Franco Mastri[3], Mauro Mongiardo[2], and Giuseppina Monti[4]

Abstract—Wireless Power Transfer (WPT) based on resonant magnetic coupling is an attractive technology for enabling the wireless recharge of electric devices and systems. One of the main drawbacks of this technology is related to the dependence of the efficiency and the power delivered to the load on possible variations of the coupling coefficient and load impedance. In order to alleviate the effects of this dependence, the optimization of appropriate adaptive matching networks is proposed in this paper. The three power gains usually adopted in the context of two-port active networks are assumed as figures of merit in the optimization process. It is theoretically and experimentally demonstrated that the maximum realizable gain of the link is achieved when the conjugate image impedance matching is realized by appropriate matching networks at both the input and output ports of the WPT link.

1. INTRODUCTION

Wireless Power Transfer based on resonant magnetic coupling has been widely investigated in the literature [1–3]. In fact, the use of a magnetic coupling allows minimizing the dependence of the performance on the surrounding environment thus making this technology particularly attractive in applications such as the recharge of medical implants or in general of embedded sensors (consider the case of structural monitoring), where the propagation channel may be subjected to variations.

Additionally, compared to conventional electromagnetic inductive coupling WPT [4], the adoption of a resonant scheme allows maximizing the performance of the WPT link and improving the robustness of the link with respect to the operating conditions.

However, although resonant inductive WPT guarantees performance nearly independent of the electromagnetic characteristics of the surrounding environment, it is quite sensitive to the coupling [2–4] and the load impedance [5–7]. The coupling dependence represents a problem for applications, such as the recharge of medical implants, where the distance may vary during the recharge process. As per the dependence on the load impedance, it is particularly critical in applications such as the recharge of a battery, where the load impedance varies during the recharge thus imposing the use of appropriate additional circuitry between the link and the battery. In order to overcome the dependence of the performance on the coupling value, the possibility of optimizing the operating frequency has been investigated in [3, 8, 9]. In particular, in [9], the use of a frequency agile scheme is proposed. The presented approach is suitable for a link operating in an over-coupling regime and consists in varying the operating frequency so to operate at the so called secondary resonances of the link. These frequencies have additional resonances which appear when the coupling coefficient of the link is higher than a critical

value. In [9] it is demonstrated that operating at the secondary resonances allows compensating the variation of the coupling coefficient due to, for instance, variations of the distance or misalignments between the two resonators. This approach operates with a generator able to track the secondary resonances of the link. Although the approach has a simple implementation, it has an important drawback of requiring operating bands determined by the range of variations of the coupling coefficient. Large ranges of variability of the coupling may lead to operating bands too wide with respect to the frequency range reserved to WPT. Additionally, as already mentioned, the frequency agile scheme is not applicable to weakly coupled WPT systems [10].

Another attractive solution, for compensating possible variations of both the coupling coefficient and load resistance, consists in using a fixed frequency approach with appropriate adaptive matching networks implemented by using either additional resonators [11–13] or lumped elements networks [14–18]. For the schemes using additional resonators (i.e., relay resonators), the adaptability of the matching network is realized by varying the mutual positions of relay elements with respect to the transmitting and receiving resonators, thus leading to a scheme difficult to implement.

As per the approaches based on lumped elements networks, an optimal resonant load transformation technique is proposed in [14]. The transformation network is implemented by using printed spiral coils and surface mounted devices, and it is designed to transform the actual load into an optimal one. In [15, 16], an automated impedance matching system where L-type and inverted L-type matching circuits are used at the input port of the link is proposed. In [17], the use of a tunable matching circuit at the transmitting side is suggested. The tunability is implemented by using a matrix of capacitors, and three different search algorithms for finding the optimum capacitance configuration are also presented. In [18], conjugate matching is realized by using two impedance matching networks, one at the input side and one at the output side. Most of these papers adopt the transmission coefficient $|S_{21}|$ for describing the performance of the link, and the various matching schemes aim at maximizing the $|S_{21}|$ parameter.

In this paper, the power gains usually adopted in the context of active networks, the power gain, available gain, and transducer gain, are used for describing the link. These three gains are expressed by well-established definitions and can be easily expressed in terms of scattering parameters. This description of the link allows avoiding the need of introducing possible misleading definitions of new variables, such as the *efficiency*, for which different definitions can be encountered in the context of WPT. Additionally, these three gains are available in common circuital simulators, which facilitate the calculation and optimization.

It is shown that the three gains are simultaneously maximized when the network is terminated on its conjugate image impedances; accordingly, the use of appropriate matching networks implementing the necessary impedance transformation for realizing this optimal condition is discussed.

The paper is organized as follows. In Section 2, the relevant gain definitions are introduced. In Section 3, the expressions of the gains in terms of scattering parameters and the condition for maximizing the performance are reported. The effect of impedance matching network is explained in Section 4, and the selection of the appropriate impedance matching network components is derived. In Section 5, the use of different impedance matching schemes is discussed. In Section 6, experimental data are reported; finally, conclusions are drawn in Section 7.

2. GAIN DEFINITIONS FOR TWO-PORT NETWORKS

In this section after introducing the analyzed case and relevant variables, the figures of merit adopted in this paper for describing the performance of the WPT link are defined.

2.1. Introduction to the Relevant Quantities According to the Impedance Matrix Representation

The case of a WPT link based on resonant inductive coupling is analyzed; accordingly, the link is modeled as a two-port network represented by the equivalent circuit illustrated in Fig. 1. It is assumed that the link is given, and it is described by its impedance parameters

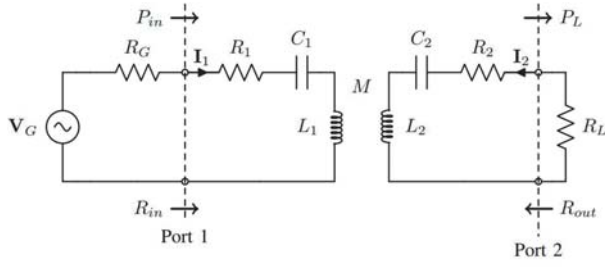$$z_{ij} = r_{ij} + jx_{ij} \tag{1}$$

Figure 1. Two-port network representation of the WPT link considered in this paper. It consists of two coupled inductances with compensating capacitances. Loss are taken into account by means of the series resistances R_1 and R_2.
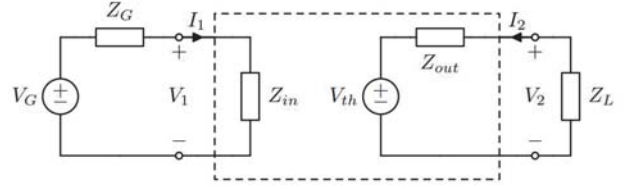
Figure 2. Equivalent circuit of a two-port network with Thevenin representation.

The general case where both the input impedance of the generator and the load could be complex quantities is considered:

$$Z_G = R_G + jX_G \tag{2a}$$
$$Z_L = R_L + jX_L \tag{2b}$$

The input impedance is derived as:

$$Z_{in} = \frac{V_1}{I_1} = z_{11} - \frac{z_{12}z_{21}}{z_{22} + Z_L}. \tag{3}$$

The voltage on the secondary side may be written as:

$$V_2 = \left(z_{22} - \frac{z_{12}z_{21}}{z_{11} + Z_G} \right) I_2 + \frac{z_{21}}{z_{11} + Z_G} V_G \tag{4}$$

which provides the following expression when the generator is short circuited:

$$Z_{out} = \left. \frac{V_2}{I_2} \right|_{V_G=0} = z_{22} - \frac{z_{12}z_{21}}{z_{11} + Z_G} = R_{out} + jX_{out} \tag{5}$$

The Thevenin equivalent voltage illustrated in Fig. 2 is readily obtained as:

$$V_{th} = V_2|_{I_2=0} = \frac{z_{21}}{z_{11} + Z_G} V_G \tag{6}$$

The input and output powers are readily evaluated as

$$P_{in} = \frac{1}{2} R_{in} |I_1|^2 \tag{7}$$

$$P_L = \frac{1}{2} R_L |I_2|^2 \tag{8}$$

The power available from the generator, P_{AG}, is given by:

$$P_{AG} = \frac{|V_G|^2}{8R_G} \tag{9}$$

while the maximum available load power P_A is:

$$P_A = \frac{|V_{th}|^2}{8R_{out}} \tag{10}$$

2.2. Figures of Merit: The Power Gains of a Two-Port Network

The figures of merit usually adopted in the context of WPT are the active power on the load and the power transfer efficiency. With regard to this last figure of merit, different definitions are available in the literature depending on whether reflections occurring at the input port are taken into account or not. In more details, in [5, 19] the efficiency is defined as:

$$\eta = \frac{P_L}{P_{in}} \tag{11}$$

where P_{in} is the power entering the two-port network expressed by Eq. (7). This definition does not take into account the power reflected toward the generator; as a consequence, in the case of links with high quality factors, it provides values of the efficiency close to 1 even with values of the power on the load close to zero [20].

A different definition has been adopted in [15, 16], where the efficiency is defined as:

$$\eta = \frac{P_L}{P_{AG}} \tag{12}$$

with P_{AG} being expressed by Eq. (9); this definition takes into account possible reflections at both the input and output ports. For given and constant values of P_{AG}, the efficiency defined as in Eq. (12) provides the same information as the active power delivered to the load.

In order to overcome the ambiguities related to the definition of the efficiency, a possible advantageous alternative description of the WPT link can be obtained by using the well-established power gain definitions commonly used for active networks: the power gain (G_P), available gain (G_A), and transducer gain (G_T) [21, 22]. The definition of these three gains and their expressions in terms of impedance matrix parameters are reported as follows.

2.2.1. Power Gain

the power gain is defined as the ratio between the power delivered to the load and the power entering the two-port network

$$G_P = \frac{P_L}{P_{in}} = \frac{R_L}{R_{in}} \left| \frac{I_2}{I_1} \right|^2 = \frac{R_L}{R_{in}} \left| \frac{z_{21}}{z_{22} + Z_L} \right|^2 \tag{13}$$

It is noted that G_P coincides with the definition of the efficiency reported in Eq. (11). Additionally, by observing the expression in terms of impedance matrix parameters, it is evident that it depends on the load impedance Z_L, while it is independent of the generator impedance Z_G.

2.2.2. Available Gain

The available power gain is defined as the ratio between the maximum available load power P_A and available input power P_{AG}

$$G_A = \frac{P_A}{P_{AG}} = \frac{R_G}{R_{out}} \left| \frac{V_{th}}{V_G} \right|^2 = \frac{R_G}{R_{out}} \left| \frac{z_{21}}{z_{11} + Z_G} \right|^2 \tag{14}$$

The available gain is only related to the generator impedance.

2.2.3. Transducer Gain

The transducer gain is defined by the relation

$$G_T = \frac{P_L}{P_{AG}} = \frac{4|z_{21}|^2 R_G R_L}{|(z_{11} + Z_G)(z_{22} + Z_L) - z_{12}z_{21}|^2} \tag{15}$$

It can be noticed that G_T coincides with the definition of the efficiency given in (12): accordingly, as already observed, for given values of P_{AG}, maximizing G_T is equivalent to maximizing the power on the load P_L.

3. SCATTERING PARAMETERS REPRESENTATION AND CONJUGATE IMAGE IMPEDANCE MATCHING CONDITION

Usually, scattering parameters are calculated and measured by using the same normalization impedance for all ports, i.e., $Z_{01} = Z_{02}$. This is mainly due to the setup commonly adopted for measurements based on the use of Vector Network Analyzers (VNAs) exhibiting a $50\,\Omega$ input impedance at all ports. However, in practical applications the two-port network is used to connect a generator having an internal impedance Z_G to a load Z_L, where, in general, Z_G and Z_L may assume complex values. Consequently, for these applications it is convenient to refer to the definition of generalized scattering parameters as introduced in [23, pp. 268–276, 24], where a different normalization impedance is assumed for each port.

Referring to Fig. 3, it is assumed that the two-port network is described by the generalized scattering parameters normalized with respect to two possibly different and complex normalization impedances Z_{01} and Z_{02}.
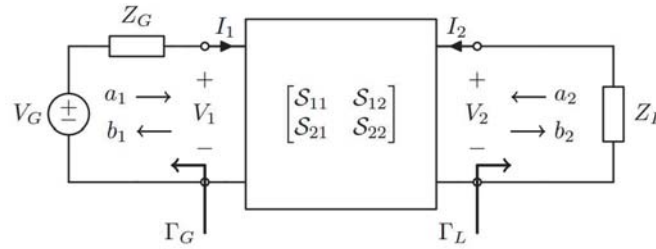

Figure 3. A two-port network represented by generalized S-parameters. It is assumed that Z_{01} and Z_{02} are the impedances adopted for normalization at port 1 and port 2, respectively.

Considering the general case where Z_{01} and Z_{02} may be different from the generator impedance Z_G and load impedance Z_L (i.e., $Z_{01} \neq Z_G$, $Z_{02} \neq Z_L$), the following expressions can be rigorously derived for the three power gains [23]:

$$G_P = \frac{|\mathcal{S}_{21}|^2(1 - |\Gamma'_L|^2)}{|1 - \mathcal{S}_{22}\Gamma'_L|^2 - |\mathcal{S}_{11} - (\mathcal{S}_{11}\mathcal{S}_{22} - \mathcal{S}_{12}\mathcal{S}_{21})\Gamma'_L|^2}, \tag{16}$$

$$G_A = \frac{(1 - |\Gamma'_G|^2)|\mathcal{S}_{21}|^2}{|1 - \mathcal{S}_{11}\Gamma'_G|^2 - |\mathcal{S}_{22} - (\mathcal{S}_{11}\mathcal{S}_{22} - \mathcal{S}_{12}\mathcal{S}_{21})\Gamma'_G|^2}, \tag{17}$$

$$G_T = \frac{(1 - |\Gamma'_G|^2)|\mathcal{S}_{21}|^2(1 - |\Gamma'_L|^2)}{|(1 - \mathcal{S}_{11}\Gamma'_G)(1 - \mathcal{S}_{22}\Gamma'_L) - \mathcal{S}_{12}\mathcal{S}_{21}\Gamma'_G\Gamma'_L|^2}. \tag{18}$$

where Γ'_G is the reflection coefficient at the input port, i.e., it accounts for the reflections between the normalization impedance Z_{01} and Z_G:

$$\Gamma'_G = \frac{Z_G - Z_{01}}{Z_G + Z_{01}^*}. \tag{19}$$

Similarly, Γ'_L is the reflection coefficient at the output port; it accounts for the reflections between the normalization impedances Z_{02} and Z_L:

$$\Gamma'_L = \frac{Z_L - Z_{02}}{Z_L + Z_{02}^*} \tag{20}$$

In the special case where $Z_{01} = Z_G$ and $Z_{02} = Z_L$, the reflection coefficients Γ'_G and Γ'_L vanish, and Eqs. (16)–(18) are reduced to [23]:

$$G_P = \frac{|\mathcal{S}_{21}|^2}{1 - |\mathcal{S}_{11}|^2} \tag{21}$$

$$G_A = \frac{|\mathcal{S}_{21}|^2}{1 - |\mathcal{S}_{22}|^2} \tag{22}$$

$$G_T = |\mathcal{S}_{21}|^2 \tag{23}$$

In general, $G_T \leq G_P$ and $G_T \leq G_A$. However, for a two-port WPT link satisfying, at both ports, the conjugate image impedance matching [25], the reflection coefficients $\mathcal{S}_{11}$ and $\mathcal{S}_{22}$ are zero, and the three gains are simultaneously maximized. In particular, the three gains assume the same value, that is the maximum realizable gain for the two-port WPT link named by Roberts the *ultimate gain*.

3.1. Conditions for Realizing the *Ultimate Gain*

The expressions of the optimal terminating impedances for maximizing the three power gains were derived by Roberts in [25]. In his pioneering work, Roberts solved the problem for a two-port network described by its impedance matrix. Starting from the scattering representation of the network, the problem can be solved as follows.

Assuming that the scattering parameters are normalized with respect to complex impedances $Z_{01} = R_{01} + jX_{01}$ and $Z_{02} = R_{02} + jX_{02}$, the following expressions relating the S-parameters to the impedance ones can be derived [26]:

$$
\begin{aligned}
\mathcal{S}_{11} &= \frac{(z_{11} - Z_{01}^*)(z_{22} + Z_{02}) - z_{12}z_{21}}{(z_{11} + Z_{01})(z_{22} + Z_{02}) - z_{12}z_{21}} \\[2mm]
\mathcal{S}_{12} &= \frac{2z_{12}(R_{01}R_{02})^{\frac{1}{2}}}{(z_{11} + Z_{01})(z_{22} + Z_{02}) - z_{12}z_{21}} \\[2mm]
\mathcal{S}_{21} &= \frac{2z_{21}(R_{01}R_{02})^{\frac{1}{2}}}{(z_{11} + Z_{01})(z_{22} + Z_{02}) - z_{12}z_{21}} \\[2mm]
\mathcal{S}_{22} &= \frac{(z_{11} + Z_{01})(z_{22} - Z_{02}^*) - z_{12}z_{21}}{(z_{11} + Z_{01})(z_{22} + Z_{02}) - z_{12}z_{21}}.
\end{aligned}
\tag{24}
$$

It is assumed that the network is reciprocal ($z_{21} = z_{12}$). In order to find the complex reference impedances Z_{c1}, Z_{c2} that annihilate both $\mathcal{S}_{11}$ and $\mathcal{S}_{22}$, the following two equations have to be solved:

$$
\begin{aligned}
(z_{11} - Z_{01}^*)(z_{22} + Z_{02}) - z_{12}^2 &= 0 \\
(z_{11} + Z_{01})(z_{22} - Z_{02}^*) - z_{12}^2 &= 0.
\end{aligned}
\tag{25}
$$

By separating the real and imaginary parts, four solving equations are obtained. The problem can be solved by introducing the auxiliary variables:

$$
\begin{aligned}
\xi^2 &= \frac{r_{12}^2}{r_{11}r_{22}} \\[2mm]
\chi^2 &= \frac{x_{12}^2}{r_{11}r_{22}},
\end{aligned}
\tag{26}
$$

which allow obtaining the desired solution:

$$
\begin{aligned}
R_{c1} &= r_{11}\sqrt{1 - \xi^2}\sqrt{1 + \chi^2} \\
R_{c2} &= r_{22}\sqrt{1 - \xi^2}\sqrt{1 + \chi^2} \\
X_{c1} &= \frac{r_{12}x_{12}}{r_{22}} - x_{11} \\
X_{c2} &= \frac{r_{12}x_{12}}{r_{11}} - x_{22}.
\end{aligned}
\tag{27}
$$

The impedances Z_{c1}, Z_{c2}:

$$
\begin{aligned}
Z_{c1} &= R_{c1} + jX_{c1}, \\
Z_{c2} &= R_{c2} + jX_{c2},
\end{aligned}
\tag{28}
$$

are the conjugate image impedances introduced by Roberts [25].

The meaning of this solution can be easily understood by a simple comparison with what is usually done with transmission lines. In fact, it is well known that in the case of a transmission line the characteristic impedance of the line has to be used as normalization impedance for making the scattering parameters related to the incident and the reflected waves along the line. Similarly, in the case of a generic two-port network, the conjugate image impedances Z_{c1} and Z_{c2} of the network are the normalization impedances that allow the generalized scattering parameters to acquire a physical meaning making them directly related to the reflections of power at various ports.

When Z_{c1} and Z_{c2} are used for normalization, that is $Z_{01} = Z_{c1}$ and $Z_{02} = Z_{c2}$, according to to Eqs. (16)–(18), the expressions of the three gains are simplified as follows:

$$G_P = \frac{|\mathcal{S}_{21}|^2(1 - |\Gamma_L'|^2)}{1 - |\mathcal{S}_{12}\mathcal{S}_{21}\Gamma_L'|^2},$$

$$G_A = \frac{(1 - |\Gamma_G'|^2)|\mathcal{S}_{21}|^2}{1 - |\mathcal{S}_{12}\mathcal{S}_{21}\Gamma_G'|^2}, \tag{29}$$

$$G_T = \frac{(1 - |\Gamma_G'|^2)|\mathcal{S}_{21}|^2(1 - |\Gamma_L'|^2)}{|(1 - \mathcal{S}_{12}\mathcal{S}_{21}\Gamma_G'\Gamma_L'|^2}.$$

The expressions given in Eq. (29) confirm that the three gains are simultaneously maximized when the conjugate image impedances of the network coincide with the generator and load impedances [25]:

$$\begin{aligned} Z_G &= Z_{c1} = R_{c1} + jX_{c1} = Z_{01}, \\ Z_L &= Z_{c2} = R_{c2} + jX_{c2} = Z_{02}. \end{aligned} \tag{30}$$

In the case where the above reported condition is satisfied, the network realizes the ultimate gain expressed by:

$$G_P = G_A = G_T = |\mathcal{S}_{21}|^2. \tag{31}$$

4. GAIN MAXIMIZATION BY IMPEDANCE MATCHING NETWORKS

4.1. Motivation of Introducing Impedance Matching Network

As already discussed, one of the most critical aspects of resonant inductive WPT is related to the dependence of the performance on the coupling coefficient, i.e., on the transfer distance. The phenomenon is illustrated in Fig. 4 where the results calculated by circuital simulations for a resonant inductive WPT link are reported. The example refers to two identical magnetically coupled inductors, and the values assumed for the inductors are the ones reported in Table 1; each inductor is loaded by a lumped capacitor realizing the resonance condition at 13.56 MHz. Fig. 4(a) shows the three gains at the
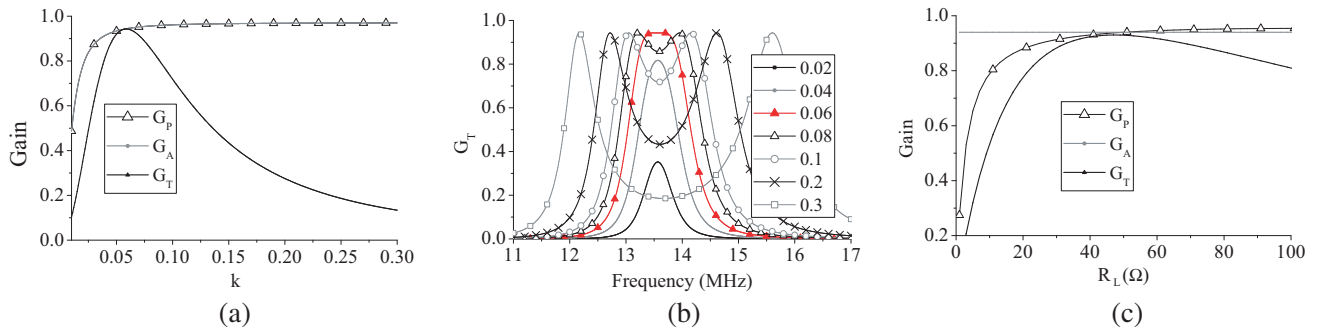

Figure 4. (a) Gains behavior for a variable coupling coefficient k. (b) Frequency characteristic of G_T for different values of k. (c) Gains behavior for a variable load impedance R_L.

Table 1. Parameters of the analyzed resonant inductive WPT link.

Inductance L (µH)	10.3
Capacitance C (pF)	13.26
Resistance R (Ω)	1.5
Operating frequency (MHz)	13.56
Q value (at 13.56 MHz)	590

main resonance (i.e., 13.56 MHz) as function of the coupling coefficient; the value assumed for R_G and R_L is 50 Ω. It can be seen that G_P and G_A continue to increase as the coupling coefficient increases, while the value assumed by G_T increases for increasing values of k until k is equal to a critical value (k_c) above which G_T begins to decrease. The behavior of G_T as function of k can also be observed in Fig. 4 which shows the frequency characteristic of G_T for different values of k. From this latter figure it can also be seen that when the link operates in an over-coupling regime, G_T exhibits two peaks around the main resonance while it exhibits a relative minimum at the main resonance. This 'split' of the absolute maximum of G_T into two distinct peaks is related to the well-known frequency splitting phenomenon which occurs for a link operating with values of the coupling coefficient above the so-called *bifurcation coupling*, k_b [9, 27]. In more details, for $k \geq k_b$, the link has three resonances, the main resonance and two secondary resonances, and the two peaks of G_T occur at two frequencies very close to, even though in general not coincident with, the secondary resonances. A possible solution in order to overcome the dependence of G_T on the coupling coefficient consists in using a frequency agile scheme where a variable operating frequency is used instead of the conventional approach using a fixed frequency [9, 28].

Another relevant problem is the dependence of the three gains on the terminating impedances (i.e., R_G and R_L) which can be observed in Fig. 4(c). In this regard, depending on the constraints imposed by the specific application of interest, two different strategies are possible [5, 29]. In the case where the link is given, it is possible to optimize the terminating impedances [5], while in the case where it is not possible to select the optimal value of R_L and R_G, it is necessary to act on the parameters of the link [29].

For given values of the link parameters and of the terminating impedances, in order to overcome the two above described issues (i.e., the dependence of the performance on k and on the terminating impedances), an attractive solution consists in using appropriate impedance matching networks (IMNs). In particular, by using one or more variable components in designing the IMNs, a nearly constant performance can be realized for a wide range of variation of k, R_L, and R_G even when the link operates at a fixed frequency.

4.2. Possible Implementations and Design of Impedance Matching Networks

The three main types of IMNs are illustrated in Fig. 5. Each IMN has to be designed for matching a given value of the impedance connected at the input port, R_G, to a given value of the impedance connected at the output port, R_L. The L-match network, see Fig. 5(a), has the simplest configuration; however, for this IMN the unloaded Q-factor of the series and parallel branches are automatically set by the resistance ratio R_G/R_L. Figure 5(b) illustrates the π-match IMN, while Fig. 5(c) illustrates the T-match IMN; these two IMNs (i.e., the pi-match and the T-match) can be considered as the combination of two L-match networks; these configurations provide more degrees of freedom for the selection of the network elements values.

Before illustrating how to design the three networks, it is convenient to introduce the series to parallel transformation illustrated in Fig. 6. The solving equation is:

$$R_s + jX_s = R_p || X_p = \frac{R_p \cdot jX_p}{R_p + jX_p} \tag{32}$$

which allows to derive the following equalities:

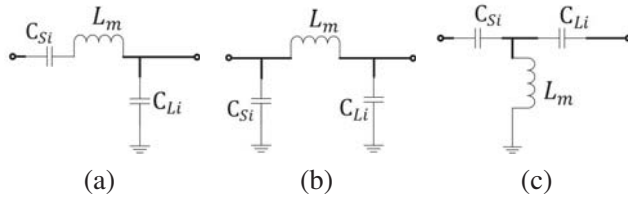$$R_s = \frac{R_p X_p^2}{R_p^2 + X_p^2} = \frac{R_p}{1 + Q^2} \tag{33}$$

Figure 5. Examples of different types of IM networks. (a) L-match. (b) π-match. (c) T-match.
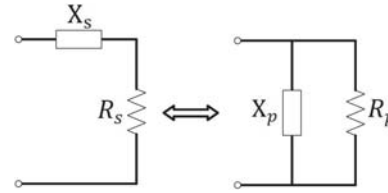

Figure 6. Series to parallel transformation.

$$R_p = R_s(1 + Q^2) \tag{34}$$

$$X_s = \frac{X_p R_p^2}{R_p^2 + X_p^2} = \frac{X_p}{1 + 1/Q^2} \tag{35}$$

$$X_p = X_s(1 + 1/Q^2).$$

where Q is the unloaded Q-factor defined as:

$$Q = R_p/X_p = X_s/R_s \tag{36}$$

From Eqs. (34) and (35), it can be seen that the equivalent resistance R_p is larger than the resistance in the series circuit R_s, while the reactances are almost the same for the two circuits since usually $Q \gg 1$.

4.3. Impedance Matching Networks Design

4.3.1. L-Match Network

Depending on whether it is necessary to transform a larger impedance to a smaller one, i.e., $R_G > R_L$, or it is necessary to transform a smaller impedance to a larger one, i.e., $R_L > R_G$, two different configurations of L-match network can be used, see Fig. 7. In the case where $R_G > R_L$, the L-match network shown in Fig. 7(a) has to be used. By using parallel to series transformation, the following relation can be derived:

$$R_G' = R_G/(1 + Q_1^2)$$
$$X_p' = X_p/(1 + 1/Q_1^2) \tag{37}$$

where Q_1 is defined as:

$$Q_1 = R_G/|X_p| = |X_p'|/R_G'. \tag{38}$$

The matching condition imposes:

$$R_G' = R_L \quad X_p' + X_s = 0$$

where R_G and R_L are given, then the quality factor can be determined by:
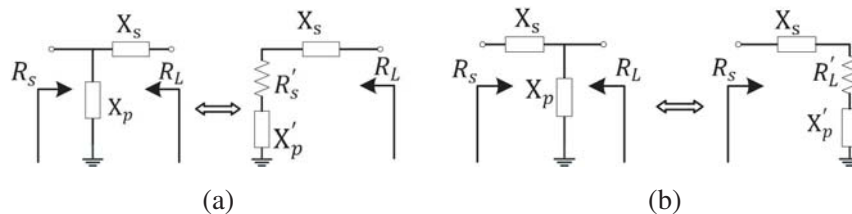
$$Q_1 = \sqrt{R_G/R_L - 1} \tag{39}$$

Figure 7. Possible configurations of L-match networks for impedance matching. (a) $R_G > R_L$. (b) $R_G < R_L$.

The parameters of the matching network are obtained in terms of Eqs. (37), (38) as follows:

$$|X_p| = R_G/Q_1$$
$$|X_s| = R_L Q_1 \quad (40)$$

In the case where $R_G < R_L$ the network to be used is the one illustrated in Fig. 7(b). Similar to what has been done for the case $R_L < R_G$, the following relations can be obtained:

$$|X_p| = R_L/\sqrt{R_L/R_G - 1}$$
$$|X_s| = R_G\sqrt{R_L/R_G - 1} \quad (41)$$

The above reported formulas are applied to the case of purely resistive values of R_G and R_L; in the case where R_G or/and R_L has/have a reactive part, it is necessary to add to the IMN appropriate compensating reactive components. For instance, when the load is complex, i.e., $Z_L = R_L + jX_L$, for the case of $R_G > R_L$, in Eq. (40) it is necessary to adjust the series component in order to compensate X_L, i.e., $X_s = \pm R_L Q_1 - X_L$.

4.3.2. π-Match Network

The π-match network, shown in Fig. 8, can be considered as the combination of two L-match networks (see Fig. 7). In order to illustrate the procedure for selecting the elements of the network, it is assumed that two IMNs, one at the input port and one at the output port, are used in order to maximize the performance of the network with respect to a generator having an impedance R_G and a load R_L. Accordingly, the π-match network at the input port has to be designed to transform the generator impedance R_G into the conjugate image impedance Z_{c1}; similarly, the π-match network at the output port has to be designed to transform the conjugate image impedance Z_{c2} into the load impedance R_L. It is observed that, in general, for a WPT link the conjugate image impedances $Z_{ci} = R_{ci} + jX_{ci}$ are complex, being purely resistive at the main resonance. The first step for calculating the elements of the IMNs consists in deriving the elements for the parallel representation of $Z_{ci} = R_{ci}^p + jX_{ci}^p$:

$$R_{ci}^p = R_{ci}\left[1 + (R_{ci}/X_{ci})^2\right]$$
$$X_{ci}^p = X_{ci}\left[1 + 1/(R_{ci}/X_{ci})^2\right] \quad (42)$$

After that, the elements of the network can be easily obtained by using the results achieved for the L-match network. In particular, for the IMN at the input (output) port, by introducing the virtual resistance R, [30, pp. 70–75] see Fig. 8, so to be smaller than either the resistance $R_G(R_L)$ or $R_{c1}(R_{c2})$, the design of the π-match network becomes equivalent to the design of the two L-match networks illustrated in Fig. 7(a). The following expressions can be derived for the network at the input port:

$$C_{s1} = \frac{\sqrt{R_G/R - 1}}{\omega R_G}$$
$$C_{L1} = \frac{\sqrt{R_{c1}^p/R - 1}}{\omega R_{c1}^p} - \frac{1}{\omega X_{c1}^p}$$
$$L_{m1} = L_{m11} + L_{m12} = R\frac{\sqrt{R_G/R - 1} + \sqrt{R_{c1}^p/R - 1}}{\omega} \quad (43)$$
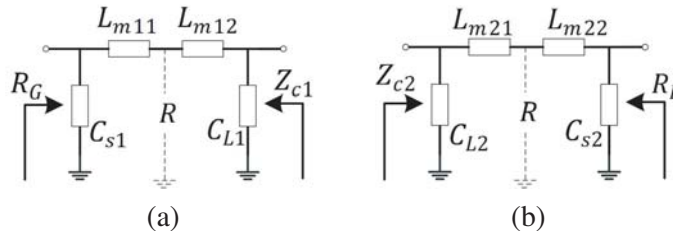

Figure 8. (a) π-match network at the input port. (b) π-match network at the output port.

For the network on the receiving side the parameters are expressed by:

$$C_{s2} = \frac{\sqrt{R_L/R - 1}}{\omega R_L}$$

$$C_{L2} = \frac{\sqrt{R_{c2}^p/R - 1}}{\omega R_{c2}^p} - \frac{1}{\omega X_{c2}^p} \tag{44}$$

$$L_{m2} = L_{m21} + L_{m22} = R\frac{\sqrt{R_L/R - 1} + \sqrt{R_{c2}^p/R - 1}}{\omega}$$

From Eqs. (43), (44), it can be seen that the values of the parameters depend on the virtual resistance R. Note that it is not necessary to choose the same R for the IMN at the input and output ports; however, for a symmetrical WPT system, the adoption of the same value for the virtual resistance R for the two IMNs leads two identical matching networks. It is worth observing that C_{s1} and C_{s2} are independent of the impedances to be realized, Z_{c1} and Z_{c2}. Additionally, since inductors introduce more losses than capacitors, their use in building the IMNs should be minimized; consequently, it is convenient to choose R so to obtain positive values for C_{L1} and C_{L2}.

5. WPT SYSTEM WITH TUNABLE IMN

In this section, based on the use of IMNs, two different schemes for improving the performance of a resonant inductive WPT link are discussed and compared. The first scheme implements a single-side matching by using a single IMN at the input port of the link (see Fig. 9(a)): the IMN is optimized for minimizing the $|S_{11}|$ parameter while maximizing the $|S_{21}|$ parameter. The second scheme adopts two IMNs in order to realize the conjugate image impedance matching at both the input and output ports (see Fig. 9(b)).
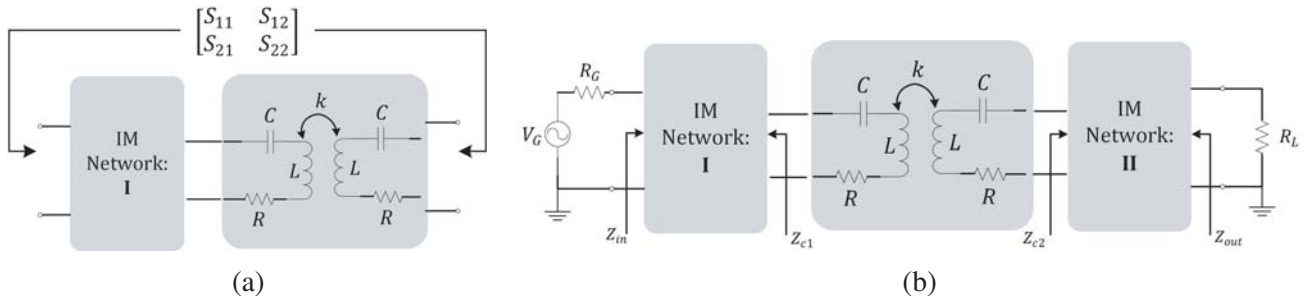

Figure 9. (a) Single-side IMN for WPT: a single IMN is present at the input port. (b) Double-side IMN for WPT: two IMNs are used for realizing the conjugate image impedance matching at both the input and the output ports.

For the sake of comparison, simulations have been performed by using the resonators presented in [15, 16]; the parameters are reported in Table 1. It is worth observing that the link does not operate at the main resonance; in fact, the operating frequency is 13.56 MHz, while, from the parameters reported in Table 1, the frequency of resonance is 13.62 MHz. As a consequence, the conjugate image impedances of the link are complex quantities. Fig. 10(a) illustrates the frequency characteristics of the three power gains of the link when no IMNs are present. The reported results have been obtained from circuital simulations performed by using the commercial tool Advanced Design System (ADS). The figures on the left refer to a high-coupling case with $k = 0.3$, while the figures on the right refers to a low-coupling case with $k = 0.03$. As can be seen, due to the frequency splitting phenomenon, for the case $k = 0.3$ the value assumed by the transducer gain at the operating frequency is very low. From theoretical formulas, the maximum realizable gain (G_u) of the analyzed WPT link is 0.99 for $k = 0.3$ and 0.89 for $k = 0.03$; according to the theory developed in Section 3, G_u is realized when the link is terminated on its conjugate image impedances. The simulated results corresponding to this optimal configuration of
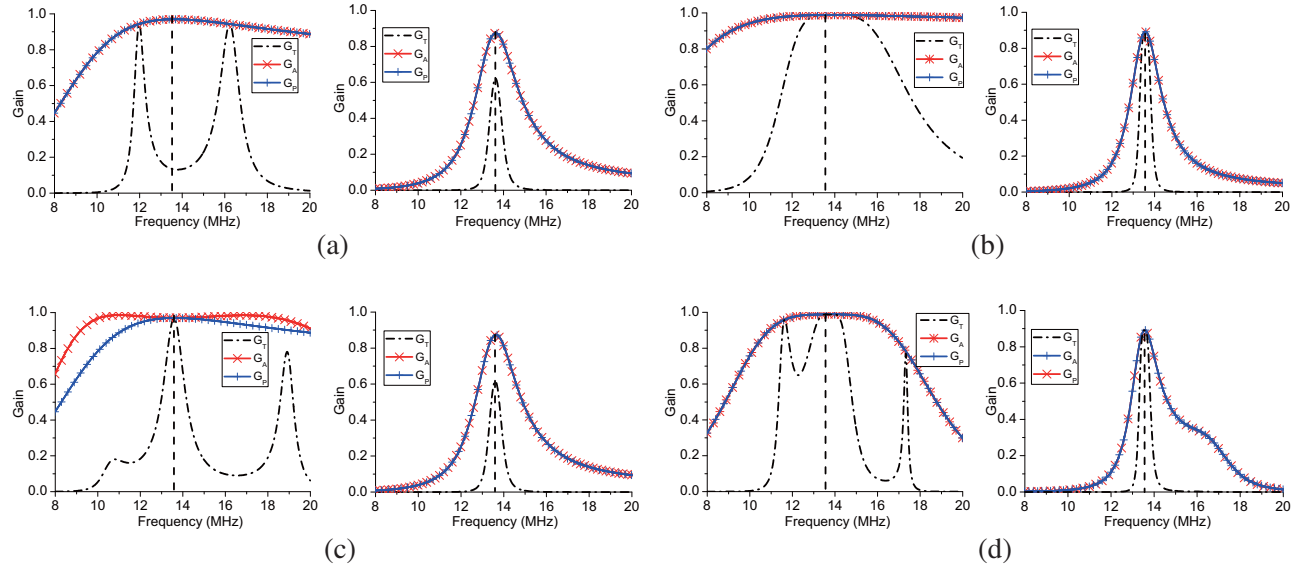
Figure 10. Frequency characteristics of the three gains of the WPT link for different IMNs schemes; the figures on the left refer to the case of $k = 0.3$, while the figures on the right refer to the case $k = 0.03$. (a) No IMN is present. (b) Frequency response of the link when it is terminated on the conjugate image impedances as defined in (28), i.e., $Z_G = Z_{c1}$ and $Z_L = Z_{c2}$. (c) Single-side matching, an L-match network is present at the input port of the link. The IMN is optimized for minimizing the $|S_{11}|$ parameter while maximizing the $|S_{21}|$ parameter. (d) Double-side matching: two π-match networks realizing the conjugate image impedance matching at the input and output ports are present. The parameters of the IMNs for the two analyzed cases (i.e., $k = 0.3$ and $k = 0.03$) are reported in Table 2 and in Table 4. (a) Non-match. (b) Ideal conjugate image impedance ended. (c) L-match network with optimization algorithm. (d) π-match network for realizing conjugate image impedance matching.

the link (i.e., for the case $Z_G = Z_{c1}$ and $Z_L = Z_{c2}$) are illustrated in Fig. 10(b) and confirm the theory; in fact, at the operating frequency the three power gains coincide and are all equal to 0.99 for the case $k = 0.3$ and to 0.89 for the case $k = 0.03$.

5.1. Single-Side Impedance Matching

The analyzed scheme is illustrated in Fig. 9(a): a single L-match network on the input side of the link is used. A value of $50\,\Omega$ is assumed for the generator and load impedances. The parameters of the IMN (i.e., L_{m1}, C_{s1}, C_{L1}) have been optimized in order to maximize the three gains which is equivalent to minimizing the $|S_{11}|$ parameter while maximizing the $|S_{21}|$ parameter. The results achieved for different values of coupling coefficient are summarized in Table 2 (see the case $R_G = R_L = 50\,\Omega$). It can be noticed that the achieved results are quite satisfactory for $k \geq 0.07$; in fact, for $k \geq 0.07$ at the operating frequency the three gains assume the same value which is very close to the maximum realizable value (i.e., G_u) reported in the last column of Table 2. It can also be seen that for $k < 0.07$, the performance achievable by using a single L-match network gets worse: the realized values for the three gains, and in particular the one realized for G_T, are lower than the maximum realizable gain.

The frequency behaviors of the three gains corresponding to the use of a single L-match network are illustrated in Fig. 10(c). The figure on the left corresponds to the high-coupling case with $k = 0.3$, while the figure on the right corresponds to the low-coupling case with $k = 0.03$. From the results reported in Fig. 10(c) it can also be observed that G_T has a peak at the operating frequency, and then it decreases very rapidly. In order to verify the dependence of these results on the specific values assumed for R_G and R_L, the cases of $R_G = R_L = 10\,\Omega$, and $R_G = 80\,\Omega$ and $R_L = 10\,\Omega$ have been analyzed. The achieved results are summarized in Table 2; obviously, G_u is the same for all the analyzed cases because it only

Table 2. Single-side matching through L-match network. Values of the components calculated by circuital simulations for different combinations of R_G and R_L.

Coupling	L_{m1} (µH)	C_{s1} (pF)	C_{L1} (pF)	G_T	G_P	G_A	G_u
		$R_G = R_L = 50\,\Omega$					
0.3	3.3	427	46	0.97	=	=	0.99
0.2	2.16	619	68	0.97	=	=	0.98
0.1	1	665	118	0.96	=	=	0.97
0.07	0.6	700	116	0.95	=	=	0.95
0.05	0.252	607	not necess.	0.92	0.93	=	0.93
0.03	0.308	575	not necess.	0.61	0.87	=	0.89
		$R_G = R_L = 10\,\Omega$					
0.3	3.17	479	49	0.87	=	0.88	0.99
0.2	2.33	333	75	0.87	=	0.88	0.98
0.1	1.3	390	155	0.87	=	0.88	0.97
0.07	1.03	364	227	0.86	=	0.88	0.95
0.05	0.72	525	328	0.86	=	0.87	0.93
0.03	0.56	431	563	0.84	=	0.86	0.89
		$R_G = 80\,\Omega,\ R_L = 10\,\Omega$					
0.3	8.35	533	18	0.87	=	0.88	0.99
0.2	5.83	282	28	0.87	=	0.88	0.98
0.1	3	280	59	0.87	=	0.88	0.97
0.07	2.86	111	86	0.86	=	0.88	0.95
0.05	0.72	525	328	0.86	=	0.87	0.93
0.03	0.25	542	103	0.81	0.84	0.81	0.89

Table 3. Single-side matching through π-network. Values of the components calculated by circuital simulations.

Coupling	L_{m1} (µH)	C_{s1} (pF)	C_{L1} (pF)	G_T	G_P	G_A	G_u
0.3	2.33	256	68	0.97	=	=	0.99
0.2	2	102	74	0.97	=	=	0.98
0.1	0.523	653	401	0.96	=	=	0.97
0.07	0.396	698	593	0.95	=	=	0.95
0.05	0.330	676	764	0.93	=	=	0.93
0.03	0.273	678	756	0.87	0.87	0.88	0.89

depends on the link. As per the values realized for the three gains by using the L-match network, it can be seen that they are more or less close to G_u depending on the values assumed for R_G and R_L.

In order to distinguish between the intrinsic limits of the single-side matching scheme and the ones related to the use of the L-match network to implement it, Table 3 summarizes the performance which can be achieved by using a single-side matching realized by a π-network. It can be seen that in this case values very close to the optimal ones are obtained for $k \geq 0.05$. However, also in this case for $k < 0.05$ the performance starts to get worse highlighting the limits of a single-side matching scheme.

5.2. Conjugate Image Impedance Matching

The theory reported in Section 3 demonstrates that the *ultimate gain* is realized when the network is conjugate matched at both ports, i.e., the network has to be terminated on $Z_G = Z_{c1}$ and $Z_L = Z_{c2}$. In order to realize the conjugate image impedance matching, it is necessary to adopt the double-side impedance matching scheme illustrated in Fig. 9(b). It is assumed that $R_G = R_L = 50\,\Omega$ and that the IMNs are realized by π-type networks. For given values of the network to be matched, and then for given values of the conjugate image impedances, the parameters of the IMNs can be calculated according to Eq. (43), (44).

The same value is assumed for the virtual resistance R of the IMN at the input port and the one at the output port; as consequence, being the analyzed WPT system symmetrical, the conjugate image impedance matching is realized by two identical networks.

Also in this case values of k in the range [0.3, 0.03] have been analyzed; for all the analyzed cases the virtual resistance R has been set to $15\,\Omega$. From theoretical formulas, the conjugate image impedance are equal to $Z_{c1} = Z_{c2} = 263.3 + j7.6\,\Omega$ for $k = 0.3$, while they are equal to $Z_{c1} = Z_{c2} = 26.4 + j7.6\,\Omega$ for $k = 0.03$. The parameters of the optimal IMNs as provided by theoretical formulas are summarized in Table 4, and the corresponding values of the three gains are also reported. As expected, the analyzed double-side matching scheme allows realizing the *ultimate gain* for each of the analyzed values of the coupling coefficient. Fig. 10(d) shows the results achieved from circuital simulations for the case $k = 0.3$ (on the left) and the case $k = 0.03$ (on the right). By comparing Fig. 10(c) and Fig. 10(d), it can be seen that the conjugate image impedance matching scheme provides decisively better performance in terms of transducer gain. In fact, for the case $k = 0.3$, it can be seen that although at the operating frequency both schemes are able to realize the optimum value, the G_T realized by the double-side matching scheme decreases more slowly in frequency. In other words, it provides a wider bandwidth. For the case $k = 0.03$, only the conjugate image impedance matching scheme realizes the optimal performance.

Table 4. Double-side matching: two π-networks, one at the input port and one at the output port, are used. Values of the components calculated by theoretical formulas. The values reported for the gains have been obtained from circuital simulations.

Coupling	L_{m1} (µH)	C_{s1} (pF)	C_{L1} (pF)	G_t	G_P	G_A	G_u
0.3	0.98	358	180	0.99	=	=	=
0.2	0.84	358	216	0.98	=	=	=
0.1	0.66	358	282	0.97	=	=	=
0.07	0.58	358	311	0.95	=	=	=
0.05	0.52	358	323	0.93	=	=	=
0.03	0.44	358	272	0.89	=	=	=

The achievable performance in the case of a variable load ia also investigated; the achieved results are summarized in Fig. 11. The figure compares the transducer gain of the link without matching with that achieved by using a single-side matching and a double-side matching. It can be noticed that by using a double-side scheme realizing the conjugate image impedance matching, a nearly constant value of G_T is obtained on a very wide range of variation of R_L.

6. EXPERIMENTAL DEMONSTRATION

In order to verify the theory presented in the previous sections, the WPT system illustrated in Fig. 12 has been arranged and experimentally analyzed. The coils are fabricated by copper wire with a diameter of $300\,\text{mm}$ and are series connected to a $120\,\text{pF}$ capacitor and a variable capacitor. The diameter of the copper wire is $2\,\text{mm}$. Table 5 summarizes the parameters (inductance and resistance) as calculated from measurements performed by using a VNA. The variable capacitors are the TZB4Z250BA10R00 by Murata, which have a capacitance range of 4–$25\,\text{pF}$; the values of these capacitors were carefully tuned in order to make the coils resonating at $13.56\,\text{MHz}$.
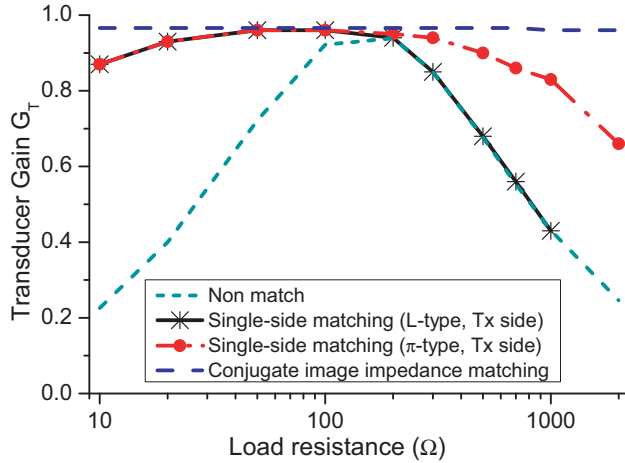
Figure 11. Transducer gain as function of the load: comparison between different optimization schemes.
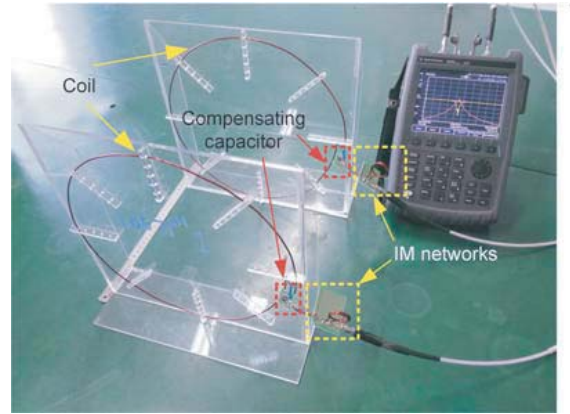

Figure 12. The experimental setup for measuring efficiency, output power and scattering parameters.

Table 5. Parameters of the fabricated coils.

TX coil inductance L_1 (μH)	1.06
RX coil inductance L_2 (μH)	1.05
TX coil resistance R_1 (Ω)	0.35
RX coil resistance R_2 (Ω)	0.4
Operating frequency (MHz)	13.56

Measurements were performed in order to verify the achievable performance when two π-networks are used for for realizing the conjugate image impedance matching. In particular, two different approaches were adopted for determining the three gains. A first set of measurements was performed by using the procedure described in [19] (see Fig. 7 of [19]) for measuring all the powers of interest for calculating the gains. In this first set of measurements data were collected for different values of the distance between the two resonators and for different values of the load. The results achieved in this way for the gains were compared with those calculated from scattering parameters. In particular, the VNA was used for measuring the scattering parameters of the link for all the configurations of interest. In this second set of measurements, the case of a variable load was realized by varying the impedance adopted for normalizing the scattering parameters at port 2.

For each specific configuration of the link, the conjugate image impedances Z_{ci} $(i = 1, 2)$ have been determined, and the components of the IMNs realizing the conjugate image impedance matching have been calculated by using Eqs. (43), (44). In this regard, it is worth observing that for the IMN at the input (output) port, the virtual resistance R has to be chosen to be smaller than the impedance to be realized, $Z_{c1}(Z_{c2})$, and the impedance $R_G(R_L)$. By denoting R_{MIN} as the lower impedance between $Z_{c1}(Z_{c2})$ and $R_G(R_L)$, the wider bandwidth is obtained by choosing the virtual resistance very close to R_{MIN}.

It should also be noticed that another critical aspect is related to the additional losses introduced by the IMNs; in this regard a key role is played by the inductors which should have a good quality factor Q.

The parameters of the IMNs for each of the analyzed configurations are reported in Table 6 for the case of a variable distance and in Table 7 for the case of a variable load. With regard to the realization of the IMNs, it should be observed that, for small variations of k or R_L, the IMNs can be implemented as reconfigurable networks by simply using two variable capacitors for C_{si} and C_{Li} and a fixed inductor in series with a variable capacitor for L_{mi}. Accordingly, the reconfigurability can be achieved by using

Table 6. Values of the elements of the IMNs for the case of a variable distance.

Distance (mm)	L_{m1} (nH)	C_{s1} (pF)	C_{L1} (pF)	L_{m2} (nH)	C_{s2} (pF)	C_{L2} (pF)
60	290	294	258	286	304	275
110	246	432	223	242	453	270
160	202	588	112	195	617	126
260	150	905	106	144	950	127
310	133	1057	108	128	1105	128

Table 7. Values of the elements of the IMNs for the case of a variable load.

R_L (Ω)	L_{m1} (nH)	C_{s1} (pF)	C_{L1} (pF)	L_{m2} (nH)	C_{s2} (pF)	C_{L2} (pF)
20	202	588	112	109	864	126
50	202	588	112	195	617	126
100	202	588	112	286	452	126
200	202	588	112	410	325	126
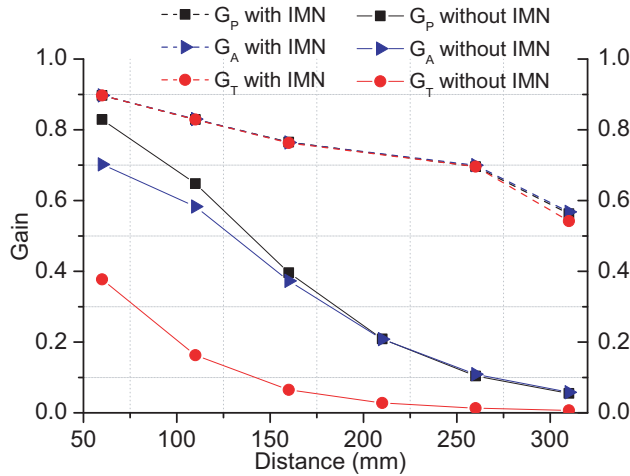
Figure 13. Measured gains achieved for the experiment illustrated in Fig. 12 by varying the distance between the two resonators. Comparison between the results achieved for the link without IMNs and those obtained by adding two π-networks realizing the conjugate image impedance matching at the input and the output ports.
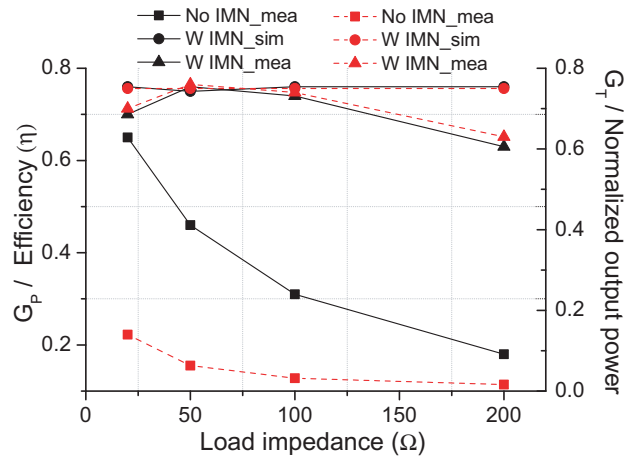
Figure 14. Results achieved by varying the load impedance. Comparison between measured data with and without IMNs. For the link with IMNs, the results achieved form circuital simulations are also reported.

only three reconfigurable capacitors. However, in the present example, the large range of variation assumed for k and R_L requires a large range of variation for the elements of the IMNs which realize the conjugate image matching for the various analyzed configurations. As a result, for the analyzed case it is not possible to cover the entire range of necessary values by simply using three variable capacitors; instead, a more complex design, such as the ones suggested in [16, 17, 31], should be adopted.

However, the focus of this paper is on validating the possibility of simultaneously maximizing the three gains by means of appropriate IMNs rather than on the design of the reconfigurable IMN. Accordingly, in order to speed up the experimental validation, measurements were performed by using different IMNs for the different analyzed cases.

In particular, the values necessary for the capacitors were realized by using a fixed capacitor

combined with the variable capacitor TZB4R500BA10R00 (capacitance range equal to 7–50 pF) by Murata, while the inductors were realized as spiral coils.

Figure 13 shows the gains calculated from measurements performed by varying the distance between the two resonators from 60 mm to 310 mm; measurements were performed with $R_G = R_L = 50\,\Omega$.

The figure compares the measured data of the link without IMNs and the ones achieved by using two IMNs. It can be observed that for small values of the distance (smaller than 60 mm) the link without matching exhibits high values of G_P and G_A but very low values of G_T. The addition of the two IMNs allows realizing the ultimate gain at all the analyzed distances, thus leading to a consistent improvement of the performance especially for increasing values of the distance. More details on the measured data of the link with and without matching are provided in Table 8.

Finally, Fig. 14 shows the achievable performance in the case where the load impedance is varied; the figure compares G_P (black) and G_T (red) of the link without IMNs and the ones corresponding to the link with IMNs. For this last case, measured data are compared with those obtained from circuital simulations by using ideal components for the IMNs. Similarly, in the case of a variable distance, a consistent improvement of the performance has been obtained by adding the two IMNs. The improvement is particularly evident for the transducer gain. However, it can be seen that the non-ideality of the components (both losses and deviation of the actual values of the components with respect to their nominal ones) leads to a performance slightly below that theoretically obtainable.

Referring to the use of matching networks for improving the performance of WPT systems, Table 9 compares the different approaches proposed in the literature and the one presented in this paper. Both [14] and [16] employed a matching network to optimize the efficiency defined as $|S_{21}|^2$. In [14], an optimal resonant load transformation with L-type network has been exploited to achieve maximum efficiency. In [16], an automated impedance matching system has been designed by minimizing S_{11}; the switches were used for selecting the specific capacitor for the matching network in Tx. The approach proposed in this paper is to explore impedance matching networks to optimize the three gains simultaneously, instead of only for transducer gain, by realizing the conjugate matching at input and output ports. As a result, all the three gains are maximized, and the network realizes the ultimate gain.

Table 8. Measured gains achieved for the experiment illustrated in Fig. 12 by varying the load impedance. Source voltage is set to 1 V, corresponding to an available input power $P_{AG} = 2.5\,\text{mW}$.

Distance (mm)		P_L (mW)	P_{in} (mW)	P_A (mW)	G_P	G_A	G_T
60	before	0.95	1.14	1.75	0.83	0.70	0.38
	after	2.24	2.5	2.24	0.9	=	=
110	before	0.41	0.63	1.46	0.65	0.58	0.16
	after	2.07	2.5	2.07	0.83	=	=
160	before	0.16	0.41	0.93	0.4	0.37	0.065
	after	1.91	2.49	1.91	0.76	=	=
260	before	0.033	0.314	0.272	0.1	0.11	0.013
	after	1.74	2.5	1.75	0.7	=	=

Table 9. Comparison with previous impedance matching method.

	Optimization	Method	Topology	Elements
[14]	Transducer gain	Matching only in Rx	L-type network	1 Capacitor and 1 inductor
[16]	Transducer gain	Matching only in Tx	L-type or inverted L-type network	19 Capacitors with matrix, 2 inductors and 21 switches
This work	Three gains	Conjugate matching both in Tx and Rx	π-type network	4 Capacitor and 2 inductors

7. CONCLUSION

The case of a WPT link based on resonant inductive coupling has been analyzed, and the possibility of compensating the dependence of the performance on the distance and on the load impedance by using appropriate matching networks has been investigated. The well-established power gain definitions commonly adopted in the context of active networks have been used for describing the link behavior. It has been shown that in order to simultaneously maximize the three power gains (i.e., the power gain, the available gain and the transducer gain) the link has to be terminated on its conjugate image impedances; as a consequence, appropriate matching networks at the input and output ports are necessary when the source and the load impedances differ from the conjugate image impedances of the link.

The results achieved for both a single-side (only one matching network at the input side) and a double-side matching scheme (two matching networks, one at the input and one at the output ports of the link) are reported. It is shown that only the double-side matching scheme guarantees the achievement of the optimal performance. However, in some cases, depending on the distance and on the terminating impedances, performance very close to the optimum can be realized also by using just one matching network. Experimental data validating the theory have been reported and discussed.

REFERENCES

1. Kurs, A., A. Karalis, R. Moffatt, J. D. Joannopoulos, P. Fisher, and M. Soljacic, "Wireless power transfer via strongly coupled magnetic resonances," *Science*, Vol. 317, No. 5834, 83–86, 2007.
2. Imura, T. and Y. Hori, "Maximizing air gap and efficiency of magnetic resonant coupling for wireless power transfer using equivalent circuit and neumann formula," *IEEE Transactions on Industrial Electronics*, Vol. 58, No. 10, 4746–4752, 2011.
3. Sample, A. P., D. T. Meyer, and J. R. Smith, "Analysis, experimental results, and range adaptation of magnetically coupled resonators for wireless power transfer," *IEEE Transactions on Industrial Electronics*, Vol. 58, No. 2, 544–554, 2011.
4. Zargham, M. and P. G. Gulak, "Maximum achievable efficiency in near-field coupled power-transfer systems," *IEEE Transactions on Biomedical Circuits & Systems*, Vol. 6, No. 3, 228–245, 2012.
5. Dionigi, M., M. Mongiardo, and R. Perfetti, "Rigorous network and full-wave electromagnetic modeling of wireless power transfer links," *IEEE Transactions on Microwave Theory and Techniques*, Vol. 63, No. 1, 65–75, Jan. 2015.
6. Monti, G., W. Che, Q. Wang, A. Costanzo, M. Dionigi, F. Mastri, M. Mongiardo, R. Perfetti, L. Tarricone, and Y. Chang, "Wireless power transfer with three-ports networks: Optimal analytical solutions," *IEEE Transactions on Circuits and Systems I: Regular Papers*, Vol. 64, No. 2, 494–503, Feb. 2017.
7. Kim, J., D. H. Kim, and Y. J. Park, "Analysis of capacitive impedance matching networks for simultaneous wireless power transfer to multiple devices," *IEEE Transactions on Industrial Electronics*, Vol. 62, No. 5, 2807–2813, 2015.
8. Kim, N. Y., K. Y. Kim, J. Choi, and C. W. Kim, "Adaptive frequency with power-level tracking system for efficient magnetic resonance wireless power transfer," *Electronics Letters*, Vol. 48, No. 8, 452–454, 2012.
9. Mastri, F., A. Costanzo, and M. Mongiardo, "Coupling-independent wireless power transfer," *IEEE Microwave and Wireless Components Letters*, Vol. 26, No. 3, 222–225, 2016.
10. Yang, Y., Y. Luo, S. Chen, and X. Wen, "A frequency-tracking and impedance-matching combined system for robust wireless power transfer," *International Journal of Antennas and Propagation*, 1–13, 2017.
11. Lee, J., Y. Lim, H. Ahn, J.-D. Yu, and S.-O. Lim, "Impedance-matched wireless power transfer systems using an arbitrary number of coils with exible coil positioning," *IEEE Antennas and Wireless Propagation Letters*, Vol. 13, 1207–1210, 2014.
12. Hoang, H., S. Lee, Y. Kim, Y. Choi, and F. Bien, "An adaptive technique to improve wireless power transfer for consumer electronics," *IEEE Transactions on Consumer Electronics*, Vol. 58, No. 2, 327–332, 2012.

13. Cannon, B. L., J. F. Hoburg, D. D. Stancil, and S. C. Goldstein, "Magnetic resonant coupling as a potential means for wireless power transfer to multiple small receivers," *IEEE Transactions on Power Electronics*, Vol. 24, No. 7, 1819–1825, 2009.

14. Xue, R.-F., K.-W. Cheng, and M. Je, "High-efficiency wireless power transfer for biomedical implants by optimal resonant load transformation," *IEEE Transactions on Circuits and Systems I: Regular Papers*, Vol. 60, No. 4, 867–874, 2013.

15. Beh, T. C., T. Imura, M. Kato, and Y. Hori, "Basic study of improving efficiency of wireless power transfer via magnetic resonance coupling based on impedance matching," *2010 IEEE International Symposium on Industrial Electronics (ISIE)*, 2011–2016, IEEE, 2010.

16. Beh, T. C., M. Kato, T. Imura, S. Oh, and Y. Hori, "Automated impedance matching system for robust wireless power transfer via magnetic resonance coupling," *IEEE Transactions on Industrial Electronics*, Vol. 60, No. 9, 3689–3698, 2013.

17. Lim, Y., H. Tang, S. Lim, and J. Park, "An adaptive impedance-matching network based on a novel capacitor matrix for wireless power transfer," *IEEE Transactions on Power Electronics*, Vol. 29, No. 8, 4403–4413, 2014.

18. Waters, B. H., A. P. Sample, and J. R. Smith, "Adaptive impedance matching for magnetically coupled resonators," *PIERS Proceedings*, 694–701, Moscow, Russia, Aug. 19–23, 2012.

19. Kiani, M., U.-M. Jow, and M. Ghovanloo, "Design and optimization of a 3-coil inductive link for efficient wireless power transmission," *IEEE Transactions on Biomedical Circuits and Systems*, Vol. 5, No. 6, 579–591, 2011.

20. Nikoletseas, S., Y. Yang, and A. Georgiadis, *Wireless Power Transfer Algorithms, Technologies and Applications in Ad Hoc Communication Networks*, Springer, 2016.

21. Mastri, F., M. Mongiardo, G. Monti, M. Dionigi, and L. Tarricone, "Gain expressions for resonant inductive wireless power transfer links with one relay element," *Wireless Power Transfer*, 2017.

22. Mastri, F., M. Mongiardo, G. Monti, and L. Tarricone, "Characterization of wireless power transfer links by network invariants," *International Conference on Electromagnetics in Advanced Applications*, 590–593, 2017.

23. Collin, R. E., *Foundations for Microwave Engineering*, McGraw-Hill, 1992.

24. Kurokawa, K., "Power waves and the scattering matrix," *IEEE Transactions on Microwave Theory and Techniques*, Vol. 13, No. 2, 194–202, 1965.

25. Roberts, S., "Conjugate-image impedances," *Proceedings of the IRE*, Vol. 34, No. 4, 198–204, 1946.

26. Frickey, D. A., "Conversions between s, z, y, h, $abcd$, and t parameters which are valid for complex source and load impedances," *IEEE Transactions on Microwave Theory and Techniques*, Vol. 42, No. 2, 205–211, Feb. 1994.

27. Niu, W.-Q., J.-X. Chu, W. Gu, and A.-D. Shen, "Exact analysis of frequency splitting phenomena of contactless power transfer systems," *IEEE Transactions on Circuits and Systems I: Regular Papers*, Vol. 60, No. 6, 1670–1677, 2013.

28. Costanzo, A., W. Che, M. Dionigi, F. Mastri, M. Mongiardo, G. Monti, L. Tarricone, and Q. Wang, "Matched resonant inductive WPT using the coupling-independent regime: Theory and experiments," *Proc. of the European Microwave Conference (EuMC)*, 204–207, 2017.

29. Monti, G., A. Costanzo, F. Mastri, M. Mongiardo, and L. Tarricone, "Rigorous design of matched wireless power transfer links based on inductive coupling," *Radio Science*, Vol. 51, No. 6, 858–867, Jun. 2016.

30. Bowick, C., *RF Circuit Design*, Sams, 1982.

31. Van Bezooijen, A., M. A. de Jongh, F. van Straten, R. Mahmoudi, and A. H. M. van Roermund, "Adaptive impedance-matching techniques for controlling L networks," *IEEE Transactions on Circuits and Systems I: Regular Papers*, Vol. 57, No. 2, 495–505, 2010.